Computational Materials Science 79 (2013) 933–943

Contents lists available at ScienceDirect

Computational Materials Science

journal homepage: www.elsevier.com/locate/commatsci

Modelling precipitate nucleation and growth with multiple precipitate species under isothermal conditions: Formulation and analysis

D. den Ouden [a,b,c,*], L. Zhao [a,c], C. Vuik [b], J. Sietsma [c], F.J. Vermolen [b]

[a] Materials innovation institute, Mekelweg 2, P.O. Box 5008, 2600 GA Delft, The Netherlands
[b] Delft University of Technology, Delft Institute of Applied Mathematics, Mekelweg 4, 2628 CD Delft, The Netherlands
[c] Delft University of Technology, Department of Materials Science and Engineering, Mekelweg 2, 2628 CD Delft, The Netherlands

ARTICLE INFO

Article history:
Received 13 February 2013
Received in revised form 18 June 2013
Accepted 26 July 2013
Available online 31 August 2013

Keywords:
KWN-model
Nucleation
Isothermal
Growth
Simulation
Multi-component
Interaction of phases

ABSTRACT

This study extends the Kampmann–Wagner-Numerical model for the nucleation and growth of precipitates. We introduce a multi-component theoretical framework for the value of the frequency of atomic attachment to a growing particle, which compares well with literature. The growth of precipitates is modelled using Zener approximations and the Gibbs–Thomson effect, where all chemical elements influence the growth rate. The model is discretised using finite-volume and time-integration techniques and subsequently applied under isothermal conditions to an industrial HSLA steel containing Nb(C,N)-, AlN- and MnS-precipitates. The simulations show the importance of the multi-component and multi-phase approach as some of the secondary phases have significant effects on other phases.

1. Introduction

Steels with higher strength and better formability are increasingly required by the automotive industry because they can provide higher safety, reduce energy consumption and thus lead to a better environmental protection. To meet these requirements, it is a sustainable effort for steel industry to develop high strength formable steels. One of the commonly used methods for such a development is micro-alloying, that is, the addition of micro-alloying elements such as niobium, vanadium and titanium at a level of only a few hundredths of a weight percent results in a very pronounced strength-enhancing effect on the steels, provided that an appropriate heat treatment is applied. It is understood that the strength-enhancing effect primarily arises from a strong reduction in the average grain size of the ferrite, originating from the grain-refining effect during the austenisation treatment. The reason for the grain-refining effect is that the micro-alloying elements have a very strong affinity for the interstitial elements such as carbon and nitrogen, leading to the precipitation of extremely fine and dispersively distributed precipitates. The existence of the precipitates prevents the growth of austenite grains by means of Zener pinning [19]. Therefore it is an essential issue for steel industry to have an accurate control of the nucleation and growth of the precipitates during thermo-mechanical processing of the steels.

The modelling of the nucleation and growth of secondary phases in the last two decades has resulted into several distinct approaches, originating from different physical origins. One of these approaches is modelling the nucleation and accompanying growth using the statistical movement of atoms within a diffusive phase, leading to a Monte Carlo method, see for example [33]. In [5] another approach is taken, which considers the time evolution of the number density of precipitates and the mean precipitate radius. Next to the first two approaches, in [15] Kampmann and Wagner introduced the modelling of a size distribution function of precipitates, which evolves using growth and nucleation laws. Within this approach two major directions can be determined: the first direction considers the time evolution of the size distribution based on Zener growth laws [39] and classical nucleation theory (CNT), see for example [24]. The second approach [35] uses also CNT for the nucleation of precipitates, but models the growth of precipitates using the thermodynamic extremum principle [21,22]. Next to the approaches modelling the simultaneous nucleation and growth, several models exist that describe the growth or dissolution of a single precipitate within a matrix [10,14,23,38]. Although these models accurately describe the growth/dissolution of a precipitate, describing the nucleation of the precipitates and a

* Corresponding author at: Materials innovation institute, Mekelweg 2, P.O. Box 5008, 2600 GA Delft, The Netherlands. Tel.: +31 152787297.
E-mail addresses: d.denouden@m2i.nl (D. den Ouden), Lie.Zhao@tudelft.nl (L. Zhao), C.Vuik@tudelft.nl (C. Vuik), J.Sietsma@tudelft.nl (J. Sietsma), F.J.Vermolen@tudelft.nl (F.J. Vermolen).

0927-0256/$ - see front matter © 2013 Elsevier B.V. All rights reserved.
http://dx.doi.org/10.1016/j.commatsci.2013.07.047

high number density of precipitates (with mutual influence) is difficult within these models.

The present paper will present a novel extended Kampmann–Wagner-Numerical (KWN) model for nucleation and growth of precipitates by Robson's formalism [28], which incorporates multi-component precipitates. These goals will be achieved by extending the formulae proposed by Robson [28] such that they account for the presence of multiple elements. A new model for the frequency of atomic attachment to a growing particle using Continuous-Time Markov-Chains will be introduced. Furthermore a multi-component growth rate description is proposed. We remark that the present paper has a theoretical and computational nature. Therefore, an experimental validation is omitted now, despite its importance on the longer term.

In the present work we will describe the model for the nucleation and growth of precipitates. Subsequently, the model will be discretised using finite-volume methods. The model and its new features will be demonstrated and compared to other models by an application to an HSLA alloy.

2. The model for multiple precipitate types, multiple elements

Nucleation and growth of precipitates can be modelled by the KWN model [28], which in the present paper will be extended in such a manner that all formulae are based on the assumption that multiple elements drive nucleation and growth of the precipitates. The main features of the standard KWN model are:

- All precipitates are spherical and classified by their radius in metres (m).
- The number balance of the model is described by the partial differential equation [12,32]:

$$\frac{\partial \phi}{\partial t} = -\frac{\partial [v\phi]}{\partial r} + S, \tag{2.1}$$

in which $\phi \equiv \phi(r,t)$ in m^{-4} represents the number density distribution of precipitates with radius r and at time t, $v \equiv v(r,t)$ in ms^{-1} represents the growth rate of precipitates with radius r and at time t. Further $S \equiv S(r,t)$ in $\mathrm{m}^{-4}\mathrm{s}^{-1}$ is a source function representing nucleation for the number density distribution of newly appearing precipitates with radius r at time t.
- The value of the source function S is calculated from CNT and is given by [12,32]

$$S(r,t) = \delta(r - r^*(t))I(t). \tag{2.2}$$

Here $I(t)$ is the nucleation rate of the precipitates following from CNT, $r^*(t)$ the critical radius following from CNT and δ the Dirac delta distribution function.
- The first-order upwind method [17] is applied to Eq. (2.1), combined with a time integration method [13].

Note that the partial differential equation given in [20], who were the first to apply the KWN-model to aluminium alloys, is given for the integrated quantity $N(r,t)$, where N represents the number density of precipitates with radius between $r - \Delta r/2$ and $r + \Delta r/2$ at time t. Myhr and Grong [20] express the relation between N and ϕ as

$$N(r,t) = \phi(r,t)\Delta r, \tag{2.3}$$

with r being taken from a set of discrete points within the range $[0,\infty)$. The right-hand side in the relation above is an approximation to the integral

$$N(r,t) = \int_{r-\Delta r/2}^{r+\Delta r/2} \phi(\tilde{r},t)\,\mathrm{d}\tilde{r}. \tag{2.4}$$

Using Eq. (2.3), N remains a discrete quantity, whereas ϕ remains continuous. This is why we have chosen to use Eq. (2.1), which is more accurate than the partial differential equation in [20]. The use of Eq. (2.1) in combination with the source function in Eq. (2.2) furthermore has the benefit that no artificial interval has to be defined in which the nucleating precipitates are added.

2.1. Extension to multiple precipitate types

In any HSLA steel, various types of precipitates can occur (see for example [6]). Consider a set of precipitate types $\mathbb{P}$, where $p \in \mathbb{P}$ stands for a type of precipitate that can occur in a specific HSLA steel. The classification of precipitate types is based on the (stoichiometric) precipitate compositions. Furthermore, let $\mathbb{E}$ be the set of elements within the HSLA steel, where $e \in \mathbb{E}$ denotes a chemical element that occurs within the HSLA steel. Then we can define the following quantities:

Nominal concentration: As the nominal concentration of an element does not depend on a precipitate type, we denote the nominal mole fraction for each element $e \in \mathbb{E}$ with $x_{0,e}$.
Mean concentration within the matrix: As the mean concentration of an element within the matrix does not depend on a specific precipitate type, we denote the mean mole fraction for each element $e \in \mathbb{E}$ by $x_{m,e}$.
Concentration within a precipitate: Within a single precipitate of type $p \in \mathbb{P}$, for each element $e \in \mathbb{E}, x_{p,e}$ denotes the mole fraction within the precipitate of type $p \in \mathbb{P}$. The related stoichiometric composition within the precipitate of type $p \in \mathbb{P}$ is denoted by $n_{p,e}$ for each element $e \in \mathbb{E}$. We stress that $x_{p,e}$ is assumed to be constant in time and position within a precipitate.

We assume that each precipitate of type $p \in \mathbb{P}$ is spherical and that it has a number density distribution $\phi_p(r,t)$. Therefore we have for each precipitate type $p \in \mathbb{P}$ a specific form of Eq. (2.1):

$$\frac{\partial \phi_p}{\partial t} = -\frac{\partial [v_p \phi_p]}{\partial r} + S_p, \tag{2.5}$$

where S_p is a source function defined as:

$$S_p(r,t) = \delta(r - r_p^*(t))I_p(t). \tag{2.6}$$

In the above equations the subscript p refers to the precipitate type p. The critical radius r_p^* and nucleation rate I_p will be defined in Section 2.2 and the growth rates v_p will be defined in Section 2.3.

2.2. Nucleation of precipitates

Following [28], we assume that the time-dependent nucleation rate I_p for precipitates of type $p \in \mathbb{P}$, as used in Eq. (2.6), is given by

$$I_p = N_{v,p} Z_p \beta_p^* \exp\left[-\frac{\Delta G_p^*}{k_B T}\right] \exp\left[-\frac{\tau_p}{t}\right], \tag{2.7}$$

where k_B and T represent the Boltzmann constant and temperature. Furthermore, $N_{v,p}$ is the number density of potential nucleation sites for precipitate type p, Z_p the Zeldovich factor, β_p^* the frequency of atomic attachment to a growing precipitate and τ_p the incubation time for precipitation, all for precipitate type p. The term ΔG_p^* is the free-energy barrier for nucleation which must be overcome before precipitation of type p occurs. The variable Z_p can be expressed by

$$Z_p = \frac{V_p^a \sqrt{\gamma_p}}{2\pi\sqrt{k_B T}} \left(\frac{1}{r_p^*}\right)^2, \tag{2.8}$$

which agrees with the equation given in [31] for spherical precipitates. In these equations V_p^a is the molecular volume of the

precipitate type p, r_p^* the critical radius of precipitate type p and γ_p the effective precipitate/matrix interface energy for precipitate type p. The incubation time τ_p is given by [31]

$$\tau_p = \frac{1}{2Z_p^2\beta_p^*}. \tag{2.9}$$

In the classical nucleation theory, the free-energy change due to a nucleation event of an incoherent spherical precipitate of type p, ΔG_p, is assumed [27] to be of the form

$$\Delta G_p = \frac{4}{3}\pi r^3 \Delta g_{v,p} + 4\pi r^2 \gamma_p. \tag{2.10}$$

In this equation, $\Delta g_{v,p}$ is the chemical free-energy change upon precipitation of precipitate type p, which has negative sign. Differentiation with respect to r and equating to zero gives the critical radius

$$r_p^* = \frac{-2\gamma_p}{\Delta g_{v,p}}, \tag{2.11}$$

with the corresponding nucleation energy barrier

$$\Delta G_p^* = \frac{4}{3}\pi\gamma_p (r_p^*)^2. \tag{2.12}$$

Following [1] and assuming a dilute solution approximation, the chemical free-energy change upon nucleation of precipitate type p can be expressed by [7]

$$\Delta g_{v,p} = -\frac{R_g T}{V_p^{\text{mole}}} \sum_{e\in\mathbb{E}_p} x_{p,e} \ln\left(\frac{x_{m,e}}{x_{m,e}^{p/m}}\right), \tag{2.13}$$

where V_p^{mole} is the molar volume of the precipitate, $x_{p,e}$ the mole fraction of element e in the precipitate, $x_{m,e}^{p/m}$ the equilibrium mole fraction of element e in the matrix at the precipitate/matrix interface and R_g the gas constant. Further, $\mathbb{E}_p \subset \mathbb{E}$ denotes the set of all chemical elements that are present in precipitate type p, that is:

$$\mathbb{E}_p = \{e \in \mathbb{E} | x_{p,e} > 0\}. \tag{2.14}$$

Appendix A shows the physical background of Eq. (2.13), which is based on the original derivation in [1] for binary systems. The mole fractions $x_{m,e}^{p/m}$ can be derived from the molar solubility product

$$\mathcal{K}_p(T) = \prod_{e\in\mathbb{E}_p} \left(x_{m,e}^{p/m}\right)^{x_{p,e}}, \tag{2.15}$$

which, in turn, is related to the commonly used solubility product

$$\mathcal{K}_p^{\%}(T) = \prod_{e\in\mathbb{E}_p} [e]^{n_{p,e}}, \tag{2.16}$$

with $[e]$ the weight percent of element e in the matrix at equilibrium.

With respect to the value of $N_{v,p}$, the number density of potential nucleation sites for an incoherent precipitate type p, see Eq. (2.7), various theories exist. One of the earliest theories by Russell [30], uses the total number of atoms per unit volume in the matrix. In [28] it is suggested to use the number of solute atoms per unit volume in the matrix, i.e. the value from [30] multiplied by the mean mole fraction of solute in the matrix. The latter approach gives a better agreement between simulations and experiments [28]. In [28] it is also suggested to replace the mole fraction of solute with an empirical parameter to match predicted and measured results. Within the computational software MatCalc [18], the number of substitutional atomic sites is used for the number density of potential nucleation sites, which is approximated by the number of substitutional sites within a matrix unit lattice cell divided by the volume of the matrix unit lattice cell. As we agree with the argument that a precipitate can nucleate at any substitutional site in the matrix lattice, we adopt the definition from [18].

The factor β^* is introduced by Robson [28] as the frequency of atomic attachment to a growing precipitate for a binary alloy with a precipitate containing a single element using the equation

$$\beta^* = \frac{4\pi D x_m}{a_m^4}(r^*)^2, \tag{2.17}$$

where D equals the bulk diffusion coefficient of the element, x_m the atomic fraction of that element in the matrix and a_m the lattice constant of the matrix. The CNT is based on the principals of nucleation theory of liquid droplets forming from a gas solution, which defines β^* as the product of the area of a spherical nucleating droplet at critical radius r_p^* and the attachment frequency of a molecule per unit area of the droplet [31]. Based on this original definition, β_p^* for a spherical precipitate type p, has the form

$$\beta_p^* = 4\pi\left(r_p^*\right)^2 \lambda_p^a, \tag{2.18}$$

with λ_p^a the effective attachment frequency of a molecule of precipitate type p per unit area. Assuming the effective attachment frequency of a precipitate molecule to be given by λ_p^m, β_p^* can be reshaped to

$$\beta_p^* = \frac{4\pi\left(r_p^*\right)^2}{a_p^2}\lambda_p^m. \tag{2.19}$$

To be able to evaluate the latter equation, we need a definition for the effective frequency λ_p^m.

A first approach that often is employed, is to apply Eq. (2.17) to the slowest diffusing element, indicating that λ_p^m is defined as

$$\lambda_p^m = \frac{D_f x_{m,f}}{a_m^2}, \tag{2.20}$$

where $f \in \mathbb{E}_p$ such that

$$D_f = \min_{e\in\mathbb{E}_p} D_e. \tag{2.21}$$

In [35] another approach is taken, in which λ_p^m is defined as

$$\lambda_p^m = \frac{1}{a_m^2\Omega}\left[\sum_{e\in\mathbb{E}_p} \frac{(c_{ke}-c_{0e})^2}{c_{0e}D_e}\right]^{-1}, \tag{2.22}$$

where the c_{ke} and c_{0e} are concentrations and Ω is the partial molar volume.[1] This approach is based on the solution of their evolution equations based on the thermodynamic extremum principle (see [21,22]) and comparison with a dilute binary system with a unary precipitate.

In the present paper, we take an atomistic approach, which will reduce to Eq. (2.17) for a binary system with a unary precipitate. Consider a precipitate type p which contains n elements, of which the first s elements are located on the substitutional lattice of the precipitate and the last $n-s$ elements are located on the interstitial lattice of the precipitate. To create an atomic unit on the surface of the precipitate, one atom of the substitutional set and one atom of the interstitial set should jump from their position in the matrix lattice to their position on the precipitate lattice. The presence of an atom of element e can be described by the state variable χ_e, which is given by

$$\chi_e = \begin{cases} 0 & \text{if atom type } e \text{ is not present,} \\ 1 & \text{if atom type } e \text{ is present,} \end{cases} \tag{2.23}$$

for $e = 1, \ldots, n$. These variables are captured in the state vector $\vec{\chi} = (\chi_1, \ldots, \chi_s | \chi_{s+1}, \ldots, \chi_n)$, which can assume 2^n different values

[1] We refer to [35] for the definitions.

at maximum. We further assume that at any time, the presence of a single element type e can change, but not simultaneously with the change of another element type. This indicates that if the state $\vec{\chi}$ of the system changes, only one χ_e changes from 0 to 1. If one of the s substitutional elements is present near the interface and simultaneously one of the $n-s$ interstitial elements is present near the interface, we assume strong bonds are created and both atoms cannot jump back to the matrix. We furthermore assume that if the system is at a state such that one substitutional and one interstitial element are present, this state cannot be left. It follows that $\vec{\chi}$ can only assume $\mathbb{S} = (s+1)(n-s+1)$ different values under these assumptions.

To model the change in the state $\vec{\chi}$, we assign to each element type e a change of energy ΔU_e when χ_e changes from 0 to 1:

$$\Delta U_e = x_{p,e}\Delta g_{v,p} V_p^{\text{mole}}. \tag{2.24}$$

These energies are based on Eq. (2.13). Now the total energy $U(\vec{\chi})$ of the state $\vec{\chi}$ can be calculated as

$$U(\vec{\chi}) = U_0 + \sum_{e=1}^{n} \chi_e \Delta U_e, \tag{2.25}$$

where U_0 is the energy of the state $(0,\ldots,0|0,\ldots,0)$. The energy difference due to the transfer from state $\vec{\chi}$ to state $\vec{\varsigma}$ can now be calculated as

$$\Delta U_{\vec{\chi}}^{\vec{\varsigma}} = U(\vec{\varsigma}) - U(\vec{\chi}) = \sum_{e=1}^{n} (\varsigma_e - \chi_e)\Delta U_e. \tag{2.26}$$

If the system is in a given state $\vec{\chi}$, we assume that it can transfer to a state $\vec{\varsigma}$ within time $t_{\vec{\chi}}^{\vec{\varsigma}}$, which is exponentially distributed with rate parameter $k_{\vec{\chi}}^{\vec{\varsigma}}$ if only a single element changes from 0 to 1 or vice versa. Following [3], we assign to such elementary state changes from $\vec{\chi}$ to $\vec{\varsigma}$ a change rate $k_{\vec{\chi}}^{\vec{\varsigma}}$ given by

$$k_{\vec{\chi}}^{\vec{\varsigma}} = \psi(f) v_{\vec{\chi}}^{\vec{\varsigma}} \frac{z}{6} \exp\left(-\frac{Q_{\vec{\chi}}^{\vec{\varsigma}} + \max(\Delta U_{\vec{\chi}}^{\vec{\varsigma}}, 0)}{R_g T}\right), \tag{2.27}$$

where f is the element that changed from 0 to 1 or vice versa and $Q_{\vec{\chi}}^{\vec{\varsigma}}$ is the activation energy for atomic jumps. The function $\psi(f)$ is given by

$$\psi(f) = \frac{1}{2}(x_{m,f}u_{p,f} - 1)(\varsigma_f - \chi_f) + \frac{1}{2}(x_{m,f}u_{p,f} + 1), \tag{2.28}$$

note that

$$\psi(f) = \begin{cases} x_{m,f}u_{p,f} & \text{if } \varsigma_f - \chi_f = 1, \\ 1 & \text{if } \varsigma_f - \chi_f = -1. \end{cases} \tag{2.29}$$

The variable $u_{p,f}$ is defined as the relative particle-lattice molar fraction of element f, given by

$$u_{p,f} = \begin{cases} \dfrac{x_{p,f}}{\sum_{e=1}^{s} x_{p,e}} & \text{if } 1 \leqslant f \leqslant s, \\ \dfrac{x_{p,f}}{\sum_{e=s+1}^{n} x_{p,e}} & \text{if } s+1 \leqslant f \leqslant n. \end{cases} \tag{2.30}$$

We have included the function $\psi(f)$ in the change rate to account for the amount of element f present in both the matrix and the precipitate. The pre-exponential frequency $v_{\vec{\chi}}^{\vec{\varsigma}}$, the vacancy concentration z, the activation energy for atomic jumps $Q_{\vec{\chi}}^{\vec{\varsigma}}$ and the average inter-atomic spacing α are related to the diffusion coefficient D_f via the approximation [27]

$$v_{\vec{\chi}}^{\vec{\varsigma}} \frac{z}{6} \exp\left(-\frac{Q_{\vec{\chi}}^{\vec{\varsigma}}}{R_g T}\right) \approx \frac{D_f}{\alpha^2}. \tag{2.31}$$

The description of the jump process fits the definition of a Continuous-Time Markov chain [29], with transition rates from Eq. (2.27). A graphical representation of this process for $n = 3$ and $s = 1$ is given in Fig. 2.1. The entire process can be captured by a transition rate matrix Q, if we assign to each state $\vec{\chi}$ a state number

$$\sigma(\vec{\chi}) = (i+1)\sum_{e=1}^{s} \chi_e e + \sum_{e=s+1}^{n} \chi_e (e-s) + 1. \tag{2.32}$$

For two different states $\vec{\chi}$ and $\vec{\varsigma}$ and associated state numbers $\sigma(\vec{\chi})$ and $\sigma(\vec{\varsigma})$ the transition matrix Q has at position $(\sigma(\vec{\chi}), \sigma(\vec{\varsigma}))$ the value

$$\begin{cases} k_{\vec{\chi}}^{\vec{\varsigma}} & \text{if } \vec{\chi} \to \vec{\varsigma} \text{ is possible}, \\ k_{\vec{\chi}}^{\vec{\varsigma}} & \text{if } \vec{\chi} \to \vec{\varsigma} \text{ is not possible}. \end{cases} \tag{2.33}$$

The diagonal of Q is such that the sum of each row of Q is zero.

Using this transition matrix Q, we can express the probabilities of being in state $i = 1,\ldots,\mathbb{S}$ at time t with the vector $\vec{p}(t) = [p_1(t), p_2(t), \ldots, p_{\mathbb{S}}(t)]$, which is given by the function

$$\vec{p}(t) = \vec{p}(0)e^{Qt}, \tag{2.34}$$

with $\vec{p}(0) = [1, 0, \ldots, 0]$. We now approximate the effective attachment frequency λ_p^m by

$$\lambda_p^m = \frac{1}{t_p^*}, \tag{2.35}$$

where t_p^* is the expected time at which we are at any of the states where one substitutional and one interstitial element are present. It can be shown that the value of t_p^* is given by

$$t_p^* = \int_0^\infty t \frac{d}{dt}\left(\sum_{j\in\mathcal{T}} p_j(t)\right) dt, \tag{2.36}$$

where $\mathcal{T}$ is the set of state where one substitutional and one interstitial element are present. If $n = 1$, so a single element e within the precipitate, we can derive the following expressions for t_p^* and β_p^*:

$$t_p^* = \frac{\alpha^2}{D_e x_{m,e}}, \tag{2.37}$$

$$\beta_p^* = \frac{4\pi\left(r_p^*\right)^2}{a_p^2} \frac{D_e x_{m,e}}{\alpha^2}, \tag{2.38}$$

which for $a_p = a_m$ and $\alpha \approx a_m$ gives the same values as Eq. (2.17).

Comparison of Eq. (2.22) with Eq. (2.35), we see that although both definitions use an effective frequency, the definition provided by [35] uses a formula related to the harmonic mean, which is frequently used to determine average frequencies. Our formulation also considers the effects of atoms jumping back and forth between the two phases, which cannot be captured correctly by assuming a harmonic mean of jump frequencies.

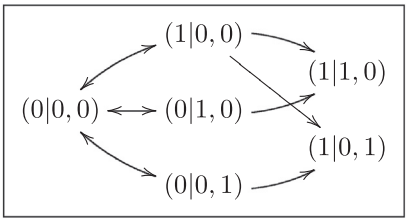

Fig. 2.1. A graphical representation of the Continuous-Time Markov chain with $n = 3$ and $s = 1$ as discussed in Section 2.2.

2.3. Growth of precipitates

In the previous section, the nucleation rates I_p, which are incorporated in the source functions S_p of Eq. (2.5), were discussed. The other factor influencing the time evolution of the precipitate distribution ϕ_p is the growth rate v_p of each precipitate with radius r. As we assume that a precipitate consists of multiple elements, we must have, following [39]

$$v_p = \frac{D_e}{r}\frac{C_{m,e} - C^{p/m,r}_{m,e}}{C_{p,e} - C^{p/m,r}_{m,e}}, \quad \forall e \in \mathbb{E}_p, \tag{2.39}$$

in which $C^{p/m,r}_{m,e}$ is the concentration[2] of element e in the matrix at the precipitate/matrix interface for precipitate type p with radius r, $C_{m,e}$ the mean concentration [2] of element e in the matrix and $C_{p,e}$ the concentration [2] of element e in the precipitate. Since a single precipitate can only grow at one defined rate, we should have

$$\frac{D_e}{r}\frac{C_{m,e} - C^{p/m,r}_{m,e}}{C_{p,e} - C^{p/m,r}_{m,e}} = \frac{D_f}{r}\frac{C_{m,f} - C^{p/m,r}_{m,f}}{C_{p,f} - C^{p/m,r}_{m,f}}, \quad \forall (e,f) \in \mathbb{E}^2_p. \tag{2.40}$$

The above system contains $|\mathbb{E}_p| - 1$ unique nonlinear equations per precipitate type p, in which $C^{p/m,r}_{m,e}, e \in \mathbb{E}_p$ are the $|\mathbb{E}_p|$ unknowns. Given a growth rate v_p, we must also have

$$\frac{D_e}{r}\frac{C_{m,e} - C^{p/m,r}_{m,e}}{-C^{p/m,r}_{m,e}} = v_p, \quad \forall e \in \mathbb{E} \setminus \mathbb{E}_p, \tag{2.41}$$

from which the concentration $C^{p/m,r}_{m,e}$ for an element e not present in the precipitate can be obtained. Define the mole fraction $x^{p/m,r}_{m,e}$ by

$$x^{p/m,r}_{m,e} = \frac{C^{p/m,r}_{m,e}}{\sum_{f\in\mathbb{E}} C^{p/m,r}_{m,f}} \quad \forall e \in \mathbb{E}. \tag{2.42}$$

If we assume that $C^{p/m,r}_{m,e}$ is influenced by surface effects, all $C^{p/m,r}_{m,e}, e \in \mathbb{E}_p$ are indirectly described by the Gibbs–Thomson effect

$$\frac{2\gamma_p V^a_p}{k_B T}\frac{1}{r} = \sum_{e\in\mathbb{E}_p} x_{p,e} \ln\left(\frac{x^{p/m,r}_{m,e}}{x^{p/m}_{m,e}}\right), \tag{2.43}$$

as was derived in [25]. Here $x^{p/m}_{m,e}$ is the local equilibrium concentration of element e in the matrix at the precipitate/matrix interface for precipitate type p. Eq. (2.43) can be recast in the form

$$\prod_{e\in\mathbb{E}_p}\left(x^{p/m,r}_{m,e}\right)^{x_{p,e}} - \mathcal{K}_p(T)\exp\left(\frac{2\gamma_p V^a_p}{k_B T}\frac{1}{r}\right) = 0, \tag{2.44}$$

where we used Eq. (2.15). The problem now reduces to finding $C^{p/m,r}_{m,e}, e \in \mathbb{E}_p$ such that Eqs. (2.40) and (2.44) hold for all $r \in [0,\infty)$ and $C^{p/m,r}_{m,e}, e \in \mathbb{E} \setminus \mathbb{E}_p$ are determined by Eq. (2.41). After solving this nonlinear problem, we obtain the concentrations $x^{p/m,r}_{m,e}$ as functions of r, then we compute $v_p(r,t)$ for one of the elements $e \in \mathbb{E}_p$, which is now the unique growth rate of a precipitate of type p with radius r at time t.

2.4. Coupling of the multiple precipitate types

Although in Sections 2.2 and 2.3 nothing was said explicitly about the manner in which different precipitate types influence each other, one can see the matrix mole fractions $x_{m,e}$ in Eqs. (2.13) and (2.28) and the matrix concentrations $C_{m,e}$ in Eqs. (2.39) and (2.41). The mole fraction within the matrix $x_{m,e}$ is related to the matrix concentrations $C_{m,e}$ by

$$x_{m,e} = \frac{C_{m,e}}{\sum_{f\in\mathbb{E}} C_{m,f}}. \tag{2.45}$$

Given the nominal molar fractions $x_{0,e}, e \in \mathbb{E}$, we can determine the nominal concentrations $C_{0,e}, e \in \mathbb{E}$ in moles per cubic metre by

$$C_{0,e} = \frac{x_{0,e}\rho}{\sum_{f\in\mathbb{E}} x_{0,f} M_f}, \tag{2.46}$$

with M_f the molar mass of element f and ρ the nominal density of the system. Then the matrix concentrations $C_{m,e}$ are given by

$$C_{m,e} = \frac{C_{0,e} - \sum_{p\in\mathbb{P}} C_{p,e} f^V_p}{1 - \sum_{p\in\mathbb{P}} f^V_p}, \tag{2.47}$$

$$\text{with } f^V_p = \int_0^\infty \frac{4}{3}\pi r^3 \phi_p \, dr, \tag{2.48}$$

$$\text{and } C_{p,e} = \frac{n_{p,e}}{V^{\text{mole}}_p}. \tag{2.49}$$

3. Numerical methods

To be able to simulate the time evolution of the solution of Eq. (2.5) for each precipitate type p, we discretise Eq. (2.5) in the precipitate radius domain and integrate in time, respectively, with the finite-volume upwind method and the Euler Implicit scheme on a fixed set of size classes. Although these two methods are theoretically first order in both time and place, we have chosen these methods as they are simple methods and they are known to preserve positivity and stability of the numerical solution unconditionally [13]. We combine these methods with a variable time-step selection, of which the details can be found in [37]. The non-linear system of equations obtained by application of the upwind method and the Euler Implicit time integration are solved using Picard's Fixed Point method.

Each Picard step requires the determination of the growth rates of each precipitate. Since the growth of the precipitate should be defined by each chemical element that is present in the precipitate, we can use Eq. (2.39) for each chemical element. This implies that Eq. (2.40) should hold for each combination of chemical elements in the precipitate. Thereby, we can express all interfacial concentrations by chosing one of them and herewith by combining Eqs. (2.40), (2.41) and (2.42), we obtain Eq. (2.44). Hence, Eq. (2.44) is solved as a single nonlinear equation for one unknown only using a quasi-Newton method.

Since we use a Picard method, combined with the aforementioned quasi-Newton method to solve the scalar Eq. (2.44), to solve the multi-variate problem arising from discretisation of Eq. (2.5) and an implicit time integration method, no numerical instabilites occured. Furthermore, we observed good convergence for both the inner quasi-Newton method and the outer Picard method at each time-step.

In [20], the size at which particles nucleate, the critical radius r^*_p, is increased by a small amount to $1.05r^*_p$, during the discretisation, to avoid numerical instability of the algorithm. A similar approach is taken within the software MatCalc [18]. The increase is physically justified as a precipitate with radius r^*_p is unlikely to grow, so it will nucleate if it is slightly larger than r^*_p. In our opinion the value with which r^*_p is increased should tend to zero as the size class length tends to zero. To this end, we determine the size class $[r_{i^*-1/2}, r_{i^*+1/2}]$, in which r^*_p is located, and replace the source function in Eq. (2.6) with

$$S_p(r,t) = \delta(r - r_{i^*+1}) I_p(t), \tag{3.1}$$

[2] In moles per cubic metre.

where r_j represents the centre of the jth size class. If we let the size class length tend to zero, the difference between the radii r_p^* and r_{i^*+1} will tend to zero, indicating that the solution of the discrete system will tend to the solution of Eq. (2.5) with the source function from Eq. (2.6). For the simulations in this paper we use a geometric mesh containing 200 size classes between the lattice parameter of each precipitate and 0.1 μm, i.e. $\Delta r_i = (1+\epsilon)\Delta r_{i-1}, i = 2, \ldots, 200$ with $\epsilon > 0$.

4. Results

In this section we simulate the precipitation kinetics in an industrial HSLA steel, of which the composition can be found in Table 4.1. Using the TCFE6 database of ThermoCalc Software AB [36] and restricting ourselves to the temperature 900 °C, we see that the primary phase is austenite and three types of precipitates occur in this steel. The precipitate types are niobium-carbonitride, aluminium-nitride and manganese-sulphide. The mole fraction for niobium in the Nb(C,N)-precipitates is given by TCFE6 database of ThermoCalc Software AB [36] as 0.5, for carbon as 0.466 and for nitrogen as 0.034. The mole fraction for aluminium and nitrogen in the AlN-precipitates as well as the mole fractions for manganese and sulphur in the MnS-precipitates are taken as 0.5. We note that $x_{Nb(C,N),C}$ depends on the solute content. However, due to the lack of the possibility to couple our code to thermodynamic databases, we take $x_{Nb(C,N),C}$ constant under isothermal conditions.

The solubility of each precipitate type is modelled using solubility products [11,9,4,34]:

$$\mathcal{K}^{\%}_{\mathrm{Nb(C,N)}} = \left(x\mathcal{K}^{\%}_{\mathrm{NbC}}\right)^{x}\left((1-x)\mathcal{K}^{\%}_{\mathrm{NbN}}\right)^{1-x}, \tag{4.1}$$

$$log_{10}\mathcal{K}^{\%}_{\mathrm{NbC}} = 3.2 - \frac{7690}{T}, \tag{4.2}$$

$$log_{10}\mathcal{K}^{\%}_{\mathrm{NbN}} = 3.57 - \frac{9660}{T}, \tag{4.3}$$

$$log_{10}\mathcal{K}^{\%}_{\mathrm{AlN}} = 1.03 - \frac{6770}{T}, \tag{4.4}$$

$$\ln \mathcal{K}_{\mathrm{MnS}} = -0.01 - \frac{1}{2}\log(2) - \frac{11282.5}{T}, \tag{4.5}$$

where x equals $2x_{\mathrm{Nb(C,N)}}$, C = 0.932. We choose the effective interfacial energies of the precipitate types as $\gamma_{\mathrm{Nb(C,N)}} = 0.19\,\mathrm{J/m^2}$, $\gamma_{\mathrm{AlN}} = 0.20\,\mathrm{J/m^2}$ and $\gamma_{\mathrm{MnS}} = 0.33\,\mathrm{J/m^2}$. These values differ from those found in literature [2,8,16], however, they fall within the range as specified in [27], and are chosen such that the simulations show the qualitative aspects of our model.

The main new features of our model are the multi-component definition of the frequency of atomic attachment, the multi-component growth rates and the coupling between the various precipitate types. First we will focus on the value of β_p^* for different approaches. Thereafter we will show the results obtained for the multi-component growth rates, in comparison with the other used growth rates (see for example [28]). Finally results from full simulations at 900 °C will be shown and discussed.

4.1. Frequency of atomic attachment

Given the composition of the steel, the solubility product and the effective interfacial energy for Nb(C,N)-precipitates, we have computed the effective frequency λ_p^m for an NbC_xN_{1-x}-precipitate at 900 °C, where the amount of carbon x in the precipitate is varied

Table 4.1
The composition of the HSLA steel in weight percent used in this article.

Element	C	Nb	N	Al	Mn	S
wt.%	0.06	0.017	0.004	0.03	0.25	0.005

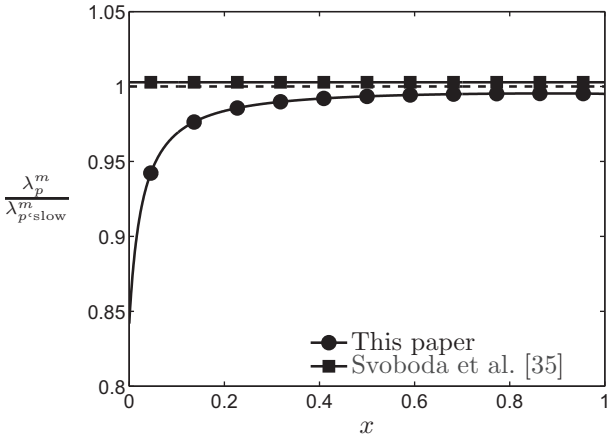

Fig. 4.1. Comparison of the effective frequencies defined by Eqs. (2.35) and (2.22) relative to Eq. (2.20) for a precipitate with stoichiometry NbC_xN_{1-x} for variable $x \in [0, 1]$.

from zero to one. Fig. 4.1 shows the results of these computations, where the horizontal axis represents the amount of carbon on the interstitial lattice and the vertical axis the ratio between the computed effective frequencies, Eqs. (2.35) and (2.22), and the effective frequency defined by the slowest element, i.e. niobium in this example, Eq. (2.20). The approach in Eq. (2.20) is referred to as the "single element approach".

From Fig. 4.1, one can see that the effective frequencies defined by [35] and defined in this paper are close to the "single element approach" which uses the slowest diffusing element, Eq. (2.20). The effective frequency calculated by the model in [35] is slightly higher than the "single element approach", whereas our approach stays below the value obtained with the single element approach. The effective frequency in [35] is strangely also less dependent on the parameter x, whereas for lower values of x, i.e. nitrogen being the more abundant element, we have a relative reduction between 5% and 15% with respect to Eq. (2.20). It is the authors' believe that the presence of any other element besides the slowest diffusing element in a precipitate should reduce the effective frequency of Eq. (2.20) by an amount, as each element should influence the effective attachment frequency of a growing precipitate. The results obtained with Eq. (2.35) reflect this property, whereas Eq. (2.22) does not. As $x \to 0^+$ and $x \to 1^-$ we should arrive at two

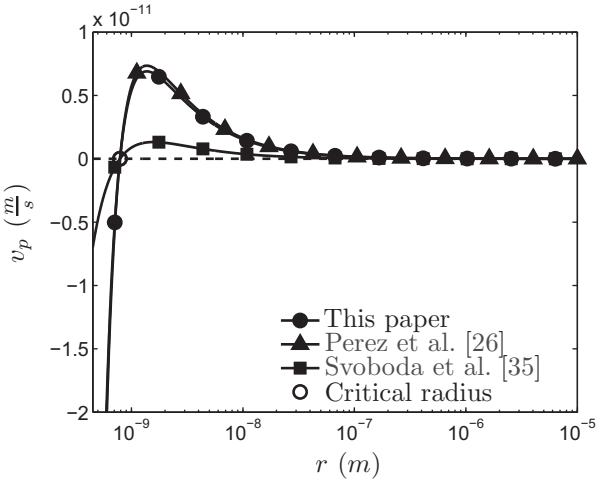

Fig. 4.2. Comparison of the various growth rate models available for an Nb(C,N)-precipitate at 900 °C.

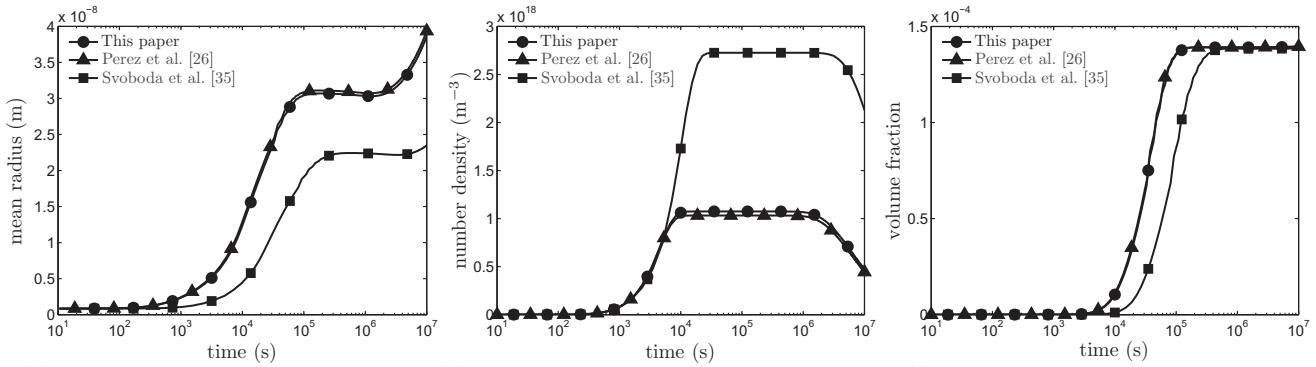

(a) The mean radius as a function of time. (b) The total number density as a function of time. (c) The volume fraction as a function of time.

Fig. 4.3. Comparison of simulation results at 900 °C between our model and the models from [26,35].

different limits, which is not reflected by applying Eqs. (2.22) and (2.20).

As our value for x equals 0.932 the different models for β_p^* will not differ more than two percent, as can be seen from Fig. 4.1. Any simulation using these values will have approximately the same quantitative results. Our model however has a richer theory than the two previously published models, which could be important in some applications.

4.2. Multi-component growth

Our multi-component model for precipitate growth differs from those found recently in literature, see [26,35]. The model in [26] uses Eqs. (2.39) and (2.44), but has replaced the concentrations in Eq. (2.39) by mole fractions with appropriate weight factors for the conversions. In this model the mole fractions are the unknowns, but do not cause a reduction in the number of unknowns. A drawback is the possibility that due to numerical errors the calculated mole fractions can be larger than one, leading to unphysical results. In our model we only have a non-negativity constraint on the unknowns, the mole fractions will always be between zero and one at all times and the sum of mole fractions equals unity at all times. The model in [35] is based on solving their evolution equations, which are based on the thermodynamic extremum principle [21,22]. Their model has an analytical solution for precipitates with constant composition, for which we refer to [35].

Fig. 4.2 shows for an Nb(C,N)-precipitate the obtained growth rates as a function of the radius at 900 °C when no precipitates have nucleated in the chosen HSLA steel. In this figure also the critical radius r_p^* is indicated. As one can see all three models provide graphs with the same shape, which all cut the zero-growth axis at the critical radius, coinciding with the theory. The model from [35] provides a significantly lower absolute value for the growth rate in comparison with our model and the model by [26] up to a radius of approximately 0.1 μm. The model from [26] shows a slightly higher value compared to our model, indicating that the model by [26] is a good approximation of our model, under the assumption that the approximation given in [39] holds. From Fig. 4.2, it is expected that the mean radii of a simulation with our model and the model from [26] increase faster in time than the mean radius obtained with the model from [35] due to the higher growth rates.

In Fig. 4.3, some results from a simulation at 900 °C for an Nb(C,N)-precipitate are shown for all three growth models.[3] Fig. 4.3(a) shows, as expected, that the mean radius of the precipitates increases faster for our model and the model from [26] than for the model from [35]. The values however have the same order of magnitude and show the same qualitative behaviour. Due to the lower growth rates in the model from [35], more solute remains available for nucleation, which causes a longer increase in the number of precipitates, as can be seen from Fig. 4.3(b). The lower growth rates cause the volume fraction to achieve its equilibrium value of 1.4088×10^{-4} at a later time with respect to the other two models, Fig. 4.3(c). All three models show nonetheless the same overall qualitative behaviour.

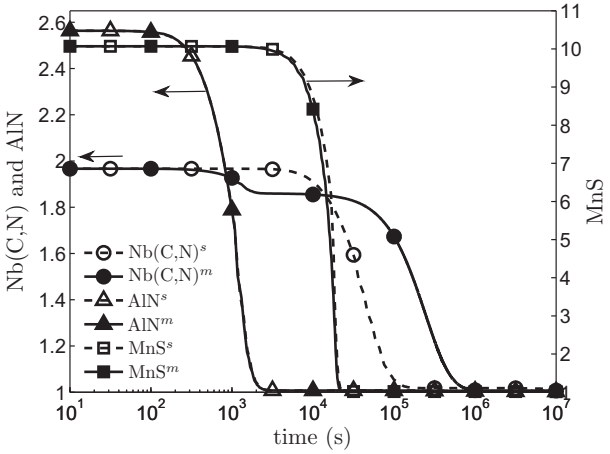

Fig. 4.4. The saturation as a function of time at 900 °C. A superscript s refers to a single-precipitate simulation, a superscript m to a multi-precipitate simulation. On the vertical axis the species for which this axis holds is given.

4.3. Interaction of multiple phases

Due to the presence of nitrogen in both the Nb(C,N)-precipitates and in the AlN-precipitates and as a result of the natural nonlinear coupling between these precipitate types as discussed in Section 2.4, we expect differences to occur in the nucleation and growth behaviour of the Nb(C,N)-precipitates and the AlN-precipitate, however not in the behaviour of the MnS-precipitates. To investigate these expected differences, we performed four simulations at 900 °C for the chosen HSLA steel, of which three simulate the nucleation and growth of each precipitate type separately and uncoupled, and one simulates the nucleation and growth of all three precipitate types simultaneously and coupled. Some of the results of these simulations are shown in Figs. 4.4 and 4.5. Fig. 4.4 shows the saturation level S_p of the matrix with respect to a precipitate type p, defined by

[3] All other formulae and discretisation techniques from this article have been used.

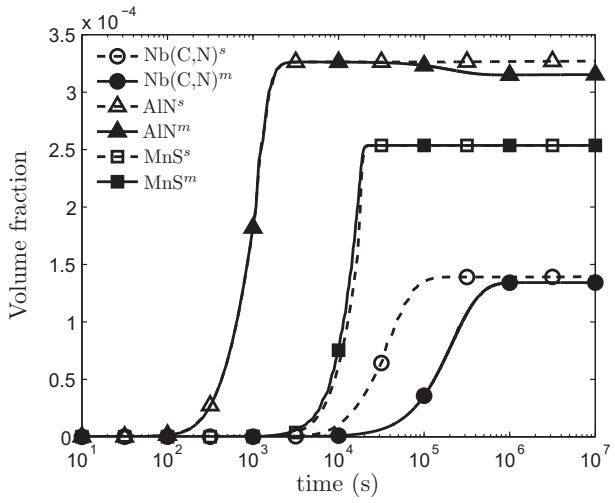

Fig. 4.5. The volume fractions as a function of time at 900 °C. A superscript *s* refers to a single-precipitate simulation, a superscript *m* to a multi-precipitate simulation.

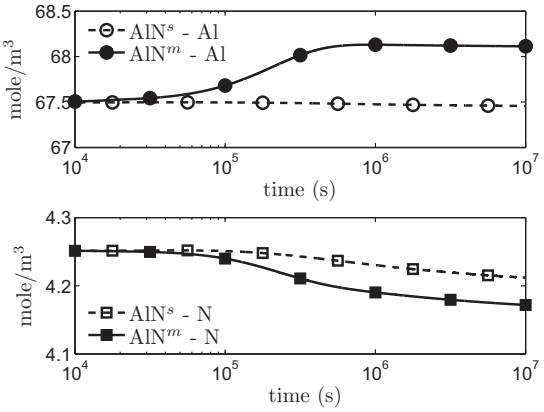

Fig. 4.7. The concentrations of aluminium and nitrogen as a function of time at 900 °C. A superscript *s* refers to a single-precipitate simulation, a superscript *m* to a multi-precipitate simulation.

$$S_p = \frac{\prod_{e\in\mathbb{E}_p}(x_{m,e})^{x_{p,e}}}{\mathcal{K}_p(T)}. \tag{4.6}$$

Fig. 4.5 depicts the time-evolution of the volume fraction of each precipitate type.

From the results in Figs. 4.4 and 4.5 it can be concluded directly that the nucleation and growth behaviour of Nb(C,N)-precipitates is sensitive to the presence of AlN-precipitates. The AlN-precipitates show a slight difference due the presence of the other precipitate types. The MnS-precipitates show no major changes with respect to the presence of the two other precipitate types. To investigate these effects further, Fig. 4.6 shows some results obtained for the Nb(C,N)-precipitates.

From Fig. 4.6(a) we can clearly see that although nucleation of Nb(C,N)-precipitates starts at approximately 100 s in both simulations, the maximum nucleation rate is reduced to about a third in the coupled approach. This reduction is caused by the decrease of nitrogen in the matrix due to the nucleated AlN-precipitates. Close inspection of the curve for the coupled simulation also shows a slight decrease in the time-derivative of the nucleation rate at about 1000 s. This decrease causes the number density of precipitates, see Fig. 4.6(b), to continue to increase longer, although a lower total number density is achieved. Due to the lower number density of precipitates, the growth of precipitates is favoured, leading to a higher mean radius, Fig. 4.6(c). We can also see that due to the longer nucleation period, no coarsening has started for the coupled simulation.

Fig. 4.5 also shows a decrease of the volume fraction of AlN after 10,000 s in the coupled simulation, which coincides with the time at which a significant fraction Nb(C,N) has been formed, Fig. 4.6(b). Inspection of Fig. 4.7 shows that at 10,000 s the matrix concentration of aluminium increases, whereas the concentration of nitrogen in the matrix decreases. The increase of the aluminium concentration can only be caused by a dissolution of AlN-precipitates, which is consistent with the decrease in the volume fraction of the AlN-precipitates. Due to the rise of the aluminium concentration in the matrix the concentration of nitrogen in the matrix must decrease for the saturation with respect to AlN-precipitates to remain at equilibrium. Since the Nb(C,N)-precipitates have not yet reached equilibrium, see Fig. 4.4, but nucleation has stopped, see Fig. 4.6(a), this decrease in nitrogen is balanced by faster growth of the Nb(C,N)-precipitates, see Fig. 4.6(c).

From the results presented in Figs. 4.4, 4.5, 4.6 and 4.7 and the above discussion, we conclude that the simultaneous simulation of multiple precipitate types can reveal the nucleation behaviour that would not have been simulated if each precipitate type would have been simulated separately. Furthermore the coupling based on the elements present within the entire system between the various precipitate types has to be taken into account.

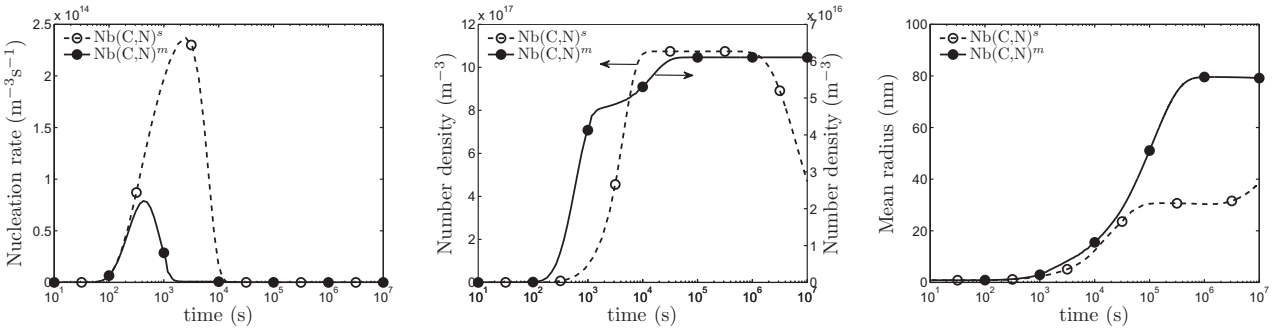

(a) The total number density as a function of time.

(b) The total number density as a function of time.

(c) The mean precipitate radius as a function of time.

Fig. 4.6. Comparison of simulation results at 900 °C for the Nb(C,N)-precipitates. A superscript *s* refers to a single-precipitate simulation, a superscript *m* to a multi-precipitate simulation.

5. Conclusions

In this article, we extended the binary KWN-model [15] for the nucleation and growth of precipitates to a model which describes nucleation and growth of multiple secondary phases, using nucleation and growth formulae depending on all elements present within the matrix and the precipitates. The time behaviour of the number density distribution has been described using a partial differential equation, where the nucleation of precipitates is given by a Dirac delta distribution function.

To incorporate a stronger dependence on the stoichiometry of the frequency of atomic attachment to a growing precipitate, we have proposed a theoretical Continuous-Time Markov-Chain based model. The model furthermore has been successfully applied to the nucleation of complex precipitates in an HSLA steel. We also note that different precipitate phases interact, which is accounted for in our model.

An improved model for the growth of precipitates has been proposed based on a molar balance on all alloying elements using the concentration in mole/m^{3}and the Gibbs–Thomson effect [25]. Use of the concentrations in mole/m^3 rather than the mole fractions as in [26] in the definition of the growth rates leads to a more accurate model, as no artificial limits on the mole fractions have to be imposed during the calculations.

We furthermore have analysed the influence of the introduced natural coupling between multiple precipitate types by application to an HSLA steel containing Nb(C,N)-, AlN- and MnS-precipitates. This analysis has shown that the coupling of the multiple phases is of importance during modelling and simulating of multiple secondary phases, as the simulations indicate that there is a mutual influence between the secondary phases during several stages of the nucleation and growth of secondary phases.

Acknowledgements

This research was carried out under the Project number M41.5.09341 in the framework of the Research Program of the Materials innovation institute M2i (www.m2i.nl).The authors wish to acknowledge the valuable input Dr. G. Hooghiemstra, Dr. C. Kraaikamp and Ir. J.S.B. van Zwieten during the discussions on the new approach for the frequency of atomic attachment to a growing precipitate.

Appendix A. Motivation of Eq. (2.13)

In [1] a plausible formula for the volume free energy density associated with precipitate nucleation in dilute solution binary alloys:

$$\Delta g_v = -\frac{R_g T}{V_p^{\text{mole}}}\left[x_p \ln\left(\frac{x_m}{x_m^{p/m}}\right) + (1-x_p)\ln\left(\frac{1-x_m}{1-x_m^{p/m}}\right)\right], \tag{A.1}$$

in which x_p refers to the mole fraction of solute in the precipitate phase p at the precipitate/matrix interface, $x_m^{p/m}$ to the mole fraction of solute in the matrix phase m at the precipitate/matrix interface and x_m to the mole fraction of solute in the matrix phase m. R, T and V_p^{mole}, respectively, are the gas constant, the absolute temperature and the molar volume of the precipitate phase. In their motivation, they restricted themselves to a binary alloy in which precipitates nucleate at a known composition. The original discussion in [1] can be adapted to calculate the volume free energy density associated with the nucleation of precipitates in a multi-component alloy, by making similar assumptions as in [1].

In the discussion in [1], the following three main assumptions are made:

1. A single precipitate has the same chemical composition as the entire precipitate phase at equilibrium.
2. The composition of the matrix phase is uniform throughout the system.
3. Only two species are present in the system, the solute and the solvent.

We now drop the third assumption, but the first two assumptions are maintained. In the remainder of the Appendix, we follow the derivation of Eq. (A.1) as originally given in [1] to motivate Eq. (2.13), which provides the multi-component equivalence of Eq. (A.1).

Assume one mole of the matrix phase m consists of $n \in \mathbb{N}$ elements with mole fractions $x_{m,e}, e \in \mathbb{E}$ for which $\sum_{e\in\mathbb{E}} x_{m,e} = 1$ and $\mathbb{E}$ is the set of atoms present within the system. From this phase, A moles of the precipitate phase p nucleate, resulting in a system containing A moles of the precipitate phase and $B = 1 - A$ moles of a new matrix phase m_1:

$$m \rightarrow Ap + Bm_1. \tag{A.2}$$

The phase p has a known and fixed composition with mole fractions $x_{p,e}, e \in \mathbb{E}$ at the precipitate/matrix interface, for which $\sum_{e\in\mathbb{E}} x_{p,e} = 1$, and the phase m_1 with resulting mole fractions $x_{m_1,e}, e \in \mathbb{E}$ for which $\sum_{e\in\mathbb{E}} x_{m_1,e} = 1$. A simple mass balance gives

$$Bx_{m_1,e} = x_{m,e} - Ax_{p,e}. \tag{A.3}$$

The volume free energy change ΔG_v associated with phase transformation (A.2) is determined by

$$\Delta G_v = AG_p + BG_{m_1} - G_m, \tag{A.4}$$

in which G_p, G_{m_1}, G_m are the molar free energies of the different phases. For any phase j, the molar free energy can be determined by the finite sum

$$G_j = \sum_{e\in\mathbb{E}} x_{j,e}\overline{G}_{j,e}, \tag{A.5}$$

where $\overline{G}_{j,e}$ represents the partial molar free energy of element e in phase j. For $j = p$ these energies are taken, similar to the related mole fractions, in phase p at the precipitate/matrix interface. Using the above formula three times in (A.4) gives

$$\Delta G_v = \sum_{e\in\mathbb{E}} Ax_{p,e}\overline{G}_{p,e} + Bx_{m_1,e}\overline{G}_{m_1,e} - x_{m,e}\overline{G}_{m,e}. \tag{A.6}$$

Due to the assumption on the composition of the precipitate being in equilibrium composition, we may replace the partial molar free energy $\overline{G}_{p,e}$ with $\overline{G}_{m,e}^{p/m}$, which is the partial molar free energy of element e in phase m at the precipitate/matrix (p/m) interface. Using this substitution and the results from the mass balance (A.3), formula (A.6) transforms to

$$\Delta G_v = \sum_{e\in\mathbb{E}} Ax_{p,e}\left(\overline{G}_{m,e}^{p/m} - \overline{G}_{m_1,e}\right) + \sum_{e\in\mathbb{E}} x_{m,e}\left(\overline{G}_{m_1,e} - \overline{G}_{m,e}\right). \tag{A.7}$$

Based on the used assumptions, we express the partial molar free energies and the molar free energies of the pure elements in the various phases in (A.7) in terms of the activities of the elements in the different phases by using the formula

$$\overline{G}_{j,e} = G_{j,e} + R_g T \ln\left(a_{j,e}\right), \tag{A.8}$$

in which $a_{j,e}$ represents the activity of element e in phase j. A superscript is introduced for $a_{j,e}$ if a specific location, being a phase or an interface, is described. Further, we assume that $G_{m,e} \approx G_{m_1,e}$. Replacing the partial molar free energies in (A.7) and rewriting gives

$$\Delta G_v = R_g TA\sum_{e\in\mathbb{E}} x_{p,e}\ln\left(\frac{a_{m,e}^{p/m}}{a_{m_1,e}}\right) + R_g T\sum_{e\in\mathbb{E}} x_{m,e}\ln\left(\frac{a_{m_1,e}}{a_{m,e}}\right). \tag{A.9}$$

Division by the number of moles A of phase p and the molar volume V_p^{mole} of phase p results in the formula

$$\Delta\tilde{g}_v = \frac{R_g T}{V_p^{\text{mole}}} \sum_{e\in\mathbb{E}} x_{p,e} \ln\left(\frac{a_{m,e}^{p/m}}{a_{m_1,e}}\right) + \frac{R_g T}{A V_p^{\text{mole}}} \sum_{e\in\mathbb{E}} x_{m,e} \ln\left(\frac{a_{m_1,e}}{a_{m,e}}\right), \tag{A.10}$$

for the volume free energy density. As A is usually small, we can take the limit of A to zero of the above formula.

First we need some preliminary calculations. Note that if we let A, the number of moles of phase p that nucleate, tend to zero, we have the following limit using (A.3) for arbitrary e:

$$\lim_{A\to 0} x_{m_1,e} = x_{m,e}. \tag{A.11}$$

Due to this limit and due to the continuity of the expression, we will also have that $a_{m_1,e} \to a_{m,e}$ as A tends to zero. Using this fact we now take the limit for A to zero of (A.10):

$$\Delta g_v = \lim_{A\to 0} \Delta\tilde{g}_v \tag{A.12}$$

$$= \lim_{A\to 0} \left[\frac{R_g T}{V_p^{\text{mole}}} \sum_{e\in\mathbb{E}} x_{p,e} \ln\left(\frac{a_{m,e}^{p/m}}{a_{m,e}}\right) + \frac{R_g T}{A V_p^{\text{mole}}} \sum_{e\in\mathbb{E}} x_{m,e} \ln\left(\frac{a_{m_1,e}}{a_{m,e}}\right) \right] \tag{A.13}$$

$$= \frac{R_g T}{V_p^{\text{mole}}} \sum_{e\in\mathbb{E}} x_{p,e} \ln\left(\frac{a_{m,e}^{p/m}}{a_{m,e}}\right) + \frac{R_g T}{V_p^{\text{mole}}} \lim_{A\to 0} \left[\frac{1}{A} \sum_{e\in\mathbb{E}} x_{m,e} \ln\left(\frac{a_{m_1,e}}{a_{m,e}}\right) \right]. \tag{A.14}$$

The latter limit is of an indeterminate form, but can be evaluated using l'Hôpital's Rule, provided the limit of the ratio of the derivatives exists:

$$= \frac{R_g T}{V_p^{\text{mole}}} \sum_{e\in\mathbb{E}} x_{p,e} \ln\left(\frac{a_{m,e}^{p/m}}{a_{m,e}}\right) + \frac{R_g T}{V_p^{\text{mole}}} \lim_{A\to 0} \left[\frac{\frac{d}{dA}\left\{ \sum_{e\in\mathbb{E}} x_{m,e} \ln\left(\frac{a_{m_1,e}}{a_{m,e}}\right) \right\}}{\frac{d}{dA}\{A\}} \right] \tag{A.15}$$

$$= \frac{R_g T}{V_p^{\text{mole}}} \sum_{e\in\mathbb{E}} x_{p,e} \ln\left(\frac{a_{m,e}^{p/m}}{a_{m,e}}\right) + \frac{R_g T}{V_p^{\text{mole}}} \lim_{A\to 0} \sum_{e\in\mathbb{E}} x_{m,e} \left[\frac{d}{dA} \left\{ \ln\left(\frac{a_{m_1,e}}{a_{m,e}}\right) \right\} \right]. \tag{A.16}$$

If we differentiate the partial molar free energy of element e in any phase j, see Eq. (A.8) with respect to A, we get

$$\frac{d\overline{G}_{j,e}}{dA} = \frac{dG_{j,e}}{dA} + R_g T \frac{d}{dA}\left[\ln\left(a_{j,e}\right)\right]. \tag{A.17}$$

Applying this to Eq. (A.16), using the definition of the derivative and pulling the summation within the limits, we get

$$\Delta g_v = \frac{R_g T}{V_p^{\text{mole}}} \sum_{e\in\mathbb{E}} x_{p,e} \ln\left(\frac{a_{m,e}^{p/m}}{a_{m,e}}\right) + \frac{1}{V_p^{\text{mole}}} \lim_{A\to 0} \lim_{\Delta A\to 0} \left[\frac{\sum_{e\in\mathbb{E}} x_{m,e} \left(\Delta\overline{G}_{m,e} - \Delta\overline{G}_{m_1,e} \right)}{\Delta A} \right]. \tag{A.18}$$

The numerator of the fraction inside the double limit can be further simplified using the Gibbs–Duhem equation, from which it follows that

$$\Delta g_v = \frac{R_g T}{V_p^{\text{mole}}} \sum_{e\in\mathbb{E}} x_{p,e} \ln\left(\frac{a_{m,e}^{p/m}}{a_{m,e}}\right) \tag{A.19}$$

$$+ \frac{1}{V_p^{\text{mole}}} \lim_{A\to 0} \lim_{\Delta A\to 0} \left[\frac{0}{\Delta A} \right], \tag{A.20}$$

which immediately gives

$$\Delta g_v = \frac{R_g T}{V_p^{\text{mole}}} \sum_{e\in\mathbb{E}} x_{p,e} \ln\left(\frac{a_{m,e}^{p/m}}{a_{m,e}}\right). \tag{A.21}$$

On basis of the dilute solution assumption we redefine (A.21) as

$$\Delta g_v = \frac{R_g T}{V_p^{\text{mole}}} \sum_{e\in\mathbb{E}} x_{p,e} \ln\left(\frac{x_{m,e}^{p/m}}{x_{m,e}}\right), \tag{A.22}$$

or equivalently

$$\Delta g_v = -\frac{R_g T}{V_p^{\text{mole}}} \sum_{e\in\mathbb{E}} x_{p,e} \ln\left(\frac{x_{m,e}}{x_{m,e}^{p/m}}\right). \tag{A.23}$$

Note that Eq. (A.23) reduces to Eq. (A.1) for a binary alloy.

References

[1] H. Aaronson, K. Kinsman, K. Russel, Scripta Metallurgica 4 (2) (1970) 101–106.
[2] K.M. Banks, A.P. Bentley, A. Koursaris, A precipitation model for predicting hot ductility behaviour in microalloyed steels, in: 42nd Mechanical Working and Steel Processing Conference, Toronto, Ontario, Canada, 2000, pp. 329–340.
[3] C. Bos, F. Sommer, E. Mittemeijer, Acta Materialia 53 (20) (2005) 5333–5341.
[4] L. Cheng, Study of the Kinetics of Precipitation, Dissolution and Coarsening of Aluminum Nitride in Low Carbon Steels, Ph.D. thesis, The University of British Columbia, 1999.
[5] A. Deschamps, Y. Brechet, Acta Materialia 47 (1) (1999) 293–305.
[6] N.H. van Dijk, S. Offerman, W. Bouwman, M. Rekveldt, J. Sietsma, S. van der Zwaag, A. Bodin, R. Heenan, Metallurgical and Materials Transactions A 33 (2002) 1883–1891.
[7] B. Dutta, J. Palmiere, C.M. Sellars, Acta Materialia 49 (2001) 785–794.
[8] T. Furuhara, J. Yamaguchi, N. Sugita, G. Miyamoto, T. Maki, ISIJ International 43 (10) (2003) 1630–1639.
[9] D. Houghton, Acta Metallurgica et Materialia 41 (10) (1993) 2993–3006.
[10] S. Hu, C.H. Henager Jr., Journal of Crystal Growth 311 (11) (2009) 3184–3194.
[11] R. Hudd, A. Jones, M. Kale, Journal of the Iron and Steel Institute 209 (1971) 121–125.
[12] H. Hulburt, S. Katz, Chemical Engineering Science 19 (8) (1964) 555–574.
[13] W. Hundsdorfer, J. Verwer, Numerical Solution of Time-Dependent Advection-Diffusion-Reaction Equations, Springer Series in Computational Mathematics, vol. 33, Springer-Verlag, Berlin Heidelberg, 2003.
[14] E. Javierre, Numerical methods for vector Stefan models of solid-state alloys, Ph.D. thesis, Delft University of Technology, 2006.
[15] R. Kampmann, R. Wagner, Materials Science and Technology – A Comprehensive Treatment, vol. 5, VCH, Weinheim, 1991.
[16] E. Kozeschnik, V. Pletenev, N. Zolotorevsky, B. Buchmayr, Metallurgical and Materials Transactions A 30 (6) (1999) 1663–1673.
[17] R.J. LeVeque, Finite Volume Methods for Hyperbolic Problems (Cambridge Texts in Applied Mathematics), Cambridge University Press, 2002.
[18] MatCalc, Institut für Werkstoffwissenschaft und Werkstofftechnologie, <http://matcalc.tuwien.ac.at>, 2012.
[19] M. Miodownik, Zener pinning, in: K. Buschow, R. Cahn, M. Flemings, B. Ilschner, E. Kramer, S. Mahajan, P. Veyssière (Eds.), Encyclopedia of Materials: Science and Technology, second ed., Elsevier, Oxford, 2001, pp. 9855–9859.
[20] O. Myhr, O. Grong, Acta Materialia 48 (7) (2000) 1605–1615.
[21] L. Onsager, Physical Review 37 (4) (1931) 405–426.
[22] L. Onsager, Physical Review 38 (12) (1931) 2265–2279.
[23] D. den Ouden, A. Segal, F.J. Vermolen, L. Zhao, C. Vuik, J. Sietsma, Computing 95 (1) (2013) 553–572.
[24] D. den Ouden, F. Vermolen, L. Zhao, C. Vuik, J. Sietsma, Computational Materials Science 50 (8) (2011) 2397–2410.
[25] M. Perez, Scripta Materialia 52 (8) (2005) 709–712.
[26] M. Perez, M. Dumont, D. Acevedo-Reyes, Acta Materialia 56 (9) (2008) 2119–2132.
[27] D. Porter, K. Easterling, Phase Transformations in Metals and Alloys, second ed., Chapmann & Hall, London UK, 1992.
[28] J. Robson, Materials Science and Technology 20 (2004) 441–448.
[29] S. Ross, Stochastic Processes. Probability and Mathematical Statistics, Wiley, 1996.
[30] K. Russell, Phase transformations, American Society for Metals, Metals Park, Ohio, 1970. p. 219.
[31] K. Russell, Advances in Colloid and Interface Science 13 (34) (1980) 205–318.

[32] S. Samaras, Modelling and Simulation in Materials Science and Engineering 14 (8) (2006) 1271–1293.
[33] F. Soisson, A. Barbu, G. Martin, Acta Materialia 44 (9) (1996) 3789–3800.
[34] W. Sun, M. Militzer, J. Jonas, Metallurgical and Materials Transactions A 23 (1992) 821–830.
[35] J. Svoboda, F. Fischer, P. Fratzl, E. Kozeschnik, Materials Science and Engineering: A 385 (2004) 166–174.
[36] TCFE6 database of ThermoCalc Software AB, TCS Steel and Fe-alloys Database. <http://www.thermocalc.com/res/pdfDBD/DBD_TCFE6.pdf>, 2010.
[37] S. van Veldhuizen, Efficient numerical methods for the instationary solution of laminar reacting gas flow problems, Ph.D. thesis, Delft University of Technology, 2009.
[38] F. Vermolen, E. Javierre, C. Vuik, L. Zhao, S. van der Zwaag, Computational Materials Science 39 (2007) 767–774.
[39] C. Zener, Journal of Applied Physics 20 (10) (1949) 950–953.